Chemical Science

ROYAL SOCIETY OF CHEMISTRY

EDGE ARTICLE

View Article Online
View Journal | View Issue

Cite this: *Chem. Sci.*, 2024, **15**, 9216

All publication charges for this article have been paid for by the Royal Society of Chemistry

Received 21st February 2024
Accepted 14th May 2024

DOI: 10.1039/d4sc01220h

rsc.li/chemical-science

Atomically dispersed dinuclear iridium active sites for efficient and stable electrocatalytic chlorine evolution reaction†

Zhipeng Yu,‡[ab] Guangjie Xia,‡[cd] Vlad Martin Diaconescu,[e] Laura Simonelli,[e] Alec P. LaGrow,[bf] Zhixin Tai,[b] Xinyi Xiang,[a] Dehua Xiong[g] and Lifeng Liu *[ab]

The electrochemical chlorine evolution reaction (CER) is a critical anode reaction in chlor-alkali electrolysis. Although precious metal-based mixed metal oxides (MMOs) have long been used as CER catalysts, they suffer from high cost and poor selectivity due to the competing oxygen evolution reaction (OER). Single-atom catalysts (SACs), featuring high atom utilization efficiency, have captured widespread interest in diverse applications. However, the single-atom sites in SACs are generally recognized as independent motifs and the interplay of adjacent sites is largely overlooked. Herein, we report a "precursor-preselected" cage-encapsulated strategy to synthesize atomically dispersed dinuclear iridium active sites bridged by oxygen that are supported on nitrogen-doped carbon (Ir_2-ONC). The dinuclear Ir_2-ONC catalyst exhibits a CER onset potential of 1.375 V *vs.* normal hydrogen electrode, a high faradaic efficiency of >95%, and a high mass activity of 14321.6 A g_{Ir}^{-1}, much better than the Ir SACs, which demonstrates the significance of coordination and electronic structure regulation for atomically dispersed catalysts. Density functional theory calculations and *ab initio* molecular dynamics simulations confirm that the unique dinuclear structure facilitates Cl^- adsorption, resulting in improved catalytic CER performance.

Chlorine (Cl_2) is one of the most important chemical commodities with an annual global production of 75 million tons.[1] It is extensively utilized in a wide range of industrial sectors, including the production of polymers and pharmaceuticals, pulp and paper industries, and water treatment.[2–4] Presently, Cl_2 is prevalently produced from the chlor-alkali process,[4,5] in which Cl_2 gas is generated *via* the electrochemical chlorine evolution reaction (CER) at the anode in an aqueous environment.[5] According to the Pourbaix diagram of the aqueous saline electrolyte, CER should be operated in acidic pH saturated with Cl^- to ensure high efficiency and production of high-purity Cl_2 gas.[5] In such harsh conditions, the catalytic materials of choice are very limited. Up to now, mixed precious metal oxides (MMOs), with a notable example of the dimensionally stable anode (DSA) consisting of IrO_2–RuO_2–TiO_2, are the best-known CER electrocatalysts with both high activity and reasonably good stability.[6,7] However, both computational and experimental results revealed that MMO catalysts are also highly active for the oxygen evolution reaction (OER), which exhibit a scaling relationship between the CER and OER,[8,9] thus leading to unsatisfactory catalytic efficiency toward the CER.[10,11] In addition, large-scale deployment of chlor-alkali electrolyzers is greatly hindered by the high demand for precious metals as anode catalysts (approximately 30 at%).[6]

From the perspective of effective utilization of noble metals, Ir and Ru based clusters are promising candidates for catalyzing the CER. To this end, some efforts have recently been made taking advantage of the metal–support interaction (MSI) to disperse and stabilize fine Ir clusters on a metal oxide support.[12,13] Notwithstanding good CER performance reported, the noble metal was not 100% utilized during electrocatalysis. To enable maximal utilization of precious metals, single-atom catalysts (SACs) have recently attracted considerable attention and been proposed to be a very promising alternative to the conventional nanoparticulate catalysts, because of their 100% atomic usage efficiency as well as unique electronic and ligand structures that can help improve catalytic performance.[14–17]

[a]*Songshan Lake Materials Laboratory, Dongguan 523808, P. R. China. E-mail: liu.lifeng@sslab.org.cn*

[b]*International Iberian Nanotechnology Laboratory (INL), Avenida Mestre Jose Veiga, 4715-330, Braga, Portugal*

[c]*School of Physical Sciences, Great Bay University, Dongguan 523808, P. R. China*

[d]*Great Bay Institute for Advanced Study, Dongguan, 523000, P. R. China*

[e]*ALBA Synchrotron, Carrer Llum 2-26, Cerdanyola del Valles, Barcelona 08290, Spain*

[f]*Scientific Imaging Section, Okinawa Institute of Science and Technology Graduate University, Kunigami-gun, Okinawa 904-0412, Japan*

[g]*State Key Laboratory of Silicate Materials for Architectures, Wuhan University of Technology, Wuhan 430070, P. R. China*

† Electronic supplementary information (ESI) available. See DOI: https://doi.org/10.1039/d4sc01220h

‡ These authors contribute equally to this work.

However, based on previous studies about CER on RuO_2 surfaces, the coordination environment around the catalytically active sites can largely influence the adsorption and desorption of Cl, thereby impacting the CER performance.[12,18,19] In such a case, isolated single-atoms, particularly those that are far away from each other, are perhaps not adequately competent in offering high activity and fast reaction kinetics for CER, and simply increasing the density of SACs on the support may readily induce nanoclustering, compromising the performance. To overcome the limitation, atomically dispersed dinuclear active sites, or double-atom catalysts, have been proposed and demonstrated to show favourable coordination and electronic structures that facilitate multiple proton/electron transfer processes, thereby enhancing catalytic activity.[20–22] Importantly, dinuclear active sites can also serve as a good model system allowing for elucidating the structure–activity relationships of catalysts. For example, Ding *et al.* reported that the dinuclear Ni_2–N_6 active sites bridged by oxygen (O–Ni_2–N_6) significantly lowered the energy barrier for CO_2 activation, and therefore were able to result in a >94% faradaic efficiency for the electroreduction of CO_2 to CO.[21] However, to the best of our knowledge, atomically dispersed dinuclear active site catalysts have been rarely exploited as an electrocatalyst for the CER so far, though some SACs were already explored recently for use in CER.[23,24]

Herein, we demonstrate the synthesis of iridium (Ir) dinuclear active sites bridged by oxygen (O) that are anchored on nitrogen doped carbon (Ir_2-ONC), which is realized using a ligand-protected dinuclear organometallic complex ($[Ir(OCH_3)(C_8H_{12})]_2$) as the metal precursor. Our aberration-corrected scanning transmission electron microscopy (STEM) and synchrotron X-ray absorption spectroscopy (XAS) characterization confirmed the dispersion of Ir_2 atomic pairs. Compared to the single-atom control catalyst (Ir_1-NC), the dinuclear metal Ir_2-ONC exhibits a much higher CER catalytic efficiency, with an onset potential of 1.375 V *vs.* the normal hydrogen electrode (NHE), which is only 44 mV higher than the standard electrode potential of the CER (E_{CER} = 1.331 V *vs.* NHE). Besides, the Ir_2-ONC shows 96.8% selectivity toward CER in acidic media at 1.42 V *vs.* NHE. Density functional theory (DFT) calculations and *ab initio* molecular dynamics (AIMD) simulations suggest that the $Ir_2O_2N_8$ configuration in Ir_2-ONC exhibits higher chloro-philicity than the Ir_1N_6 configuration in Ir_1-NC, and therefore shows a lower Cl substitution-coordination free energy, which rationally explains the higher activity observed for Ir_2-ONC. *In situ* Raman spectroscopy investigation also confirms the higher chloro-philicity of the Ir_2-ONC catalysts.

As detailed in Experimental section, Ir dinuclear active sites were constructed through a "precursor-preselected" cage-encapsulated strategy, where the organometallic complex (1,5-cyclooctadiene)(methoxy)iridium(I) ($[Ir(OCH_3)(C_8H_{12})]_2$) comprising an Ir dinuclei was used as the precursor and zeolite imidazolate framework 8 (ZIF-8) as the host to *in situ* encapsulate Ir dimers through the space-confinement effect and abundant uncoordinated nitrogen-containing groups. A subsequent pyrolysis led to the formation of chemical bonds between Ir and N, hence the atomically dispersed Ir dinuclear active sites become embedded in the derived carbon framework (Ir_2-ONC). For comparison, the Ir_1-NC catalyst containing singly dispersed atomic active sites of Ir were also prepared as a control through a similar method, but using Ir acetylacetonate ($Ir(acac)_3$) as the Ir precursor. The high-angle annular dark-field scanning transmission electron microscopy (HAADF-STEM) examination confirmed successful synthesis of nitrogen-doped carbon (NC), Ir_1-NC and Ir_2-ONC, which all show uniform sizes and well-defined dodecahedral shape (Fig. 1a, S1, and S2a, ESI†). X-ray diffraction (XRD) measurements did not reveal any characteristic diffraction peaks of metallic Ir and/or its compounds in Ir_1-NC and Ir_2-ONC, confirming no agglomeration of Ir atoms during the pyrolysis process (Fig. S3, ESI†). The morphology and microstructure of Ir_2-ONC were further examined by HAADF-STEM. As shown in Fig. 1b and c, bright spots can be clearly discerned, corresponding to the dispersed Ir metal atoms. A closer inspection (Fig. 1c) further corroborates the presence of spatially proximate Ir dimers (marked with yellow circles), which are believed to derive from the dinuclei in $[Ir(OCH_3)(C_8H_{12})]_2$ precursors. STEM elemental mapping further demonstrated that Ir is distributed evenly on NC (Fig. 1d). It is also noted that some Ir atoms are existent individually without a neighboring atom. This may result from the high-temperature pyrolysis process, during which the bond between two Ir dinuclei was broken. We managed to optimize the pyrolysis conditions, but singly dispersed Ir atoms were always found in all cases. We notice that in previously reported diatomic catalysts, singly dispersed atoms also parasitically appeared. In fact, synthesizing dinuclear active sites with a 100% yield is currently still an unmet challenge.

Besides, the morphology and microstructure of Ir_1-NC control catalysts were also characterized by HAADF-STEM (Fig. S2, ESI†), and the atomic dispersion of Ir was unambiguously confirmed. The N_2 adsorption/desorption isotherms (Fig. S4a, ESI†) indicate that the specific surface area of Ir_2-NC is 842.5 $m^2\ g^{-1}$, larger than that of other control catalysts (551.3 $m^2\ g^{-1}$ for NC and 691.8 $m^2\ g^{-1}$ for Ir_1-NC), suggesting that the introduction of Ir dimers is beneficial to expose more active

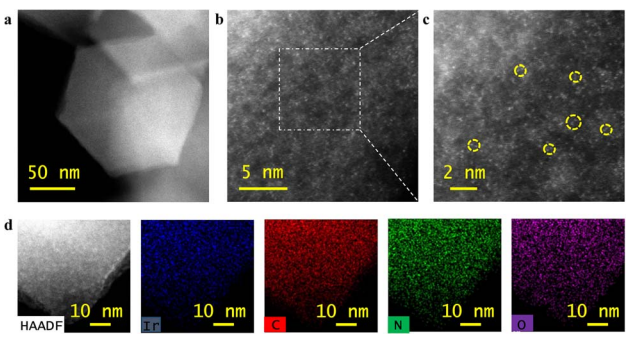

Fig. 1 Morphology and microstructure characterization of Ir_2-ONC catalysts. (a) HAADF-STEM image. (b and c) High-resolution HAADF-STEM images. In panel (c), some representative Ir_2 dinuclear sites are marked with yellow circles. (d) HAADF-STEM image and the corresponding elemental maps of Ir, C, N and O.

sites. Raman spectroscopy measurements (Fig. S4b, ESI†) suggest the presence of abundant disordered graphitic carbon, as evidenced by the relatively high intensity ratio of the D peak over G peak (I_D/I_G), which may arise from the high degree of microporosity as revealed by the sorption isotherm and also likely relate to the etching effect of metals during the carbonization.[20] Furthermore, the Ir content for Ir_1-NC and Ir_2-ONC was determined to be ~0.45 wt% and 0.61 wt%, respectively, according to the inductively coupled plasma optical emission spectrometry (ICP-OES) analysis (Fig. S5, ESI†).

X-ray photoelectron spectroscopy (XPS) was conducted to characterize the surface chemistry and composition of the catalysts. The XPS survey spectra of samples confirm the presence of corresponding elements in each catalyst, as shown in Fig. S6 (ESI†). The quantitative XPS analysis revealed that there is 1.12 at%, 1.54 at%, and 1.38 at% Zn in NC, Ir_1-NC, and Ir_2-ONC, respectively, which is derived from the residue of Zn in ZIF-8 precursor.[25,26] It is expected that such little amount of Zn will not markedly influence electrocatalytic activity. The high-resolution N 1s spectra of NC, Ir_1-NC and Ir_2-ONC are shown in Fig. 2a. The N 1s XPS spectrum of NC can be de-convoluted into four components, corresponding to pyridinic-N (398.3 eV), pyrrolic-N (399.7 eV), graphitic-N (400.9 eV) and oxyl-N (404.8 eV),[27,28] respectively. Besides these functional groups, metal–nitrogen (M–N) bonding at 399.0 eV is observed in both Ir_1-NC and Ir_2-ONC samples, implying that the uncoordinated N groups serve as the anchoring points of metal species forming Ir–N bonding, consistent with previous reports.[20,29,30] XPS

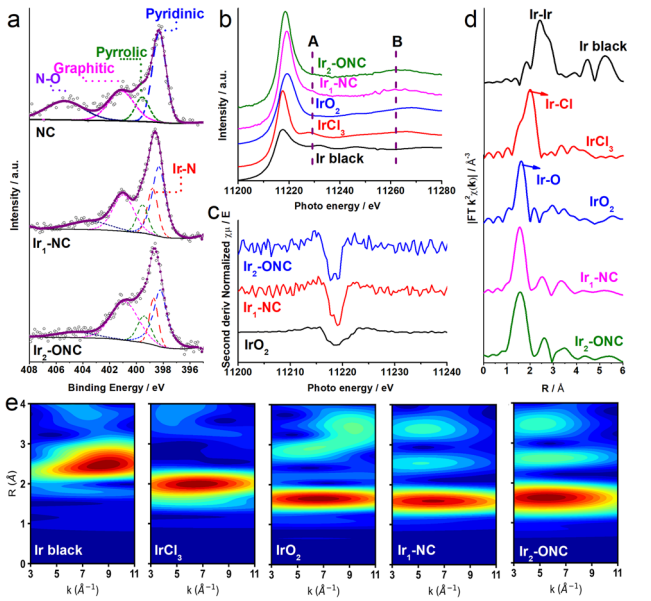

Fig. 2 Electronic structure analyses of Ir_2-ONC and other control samples. (a) High-resolution N 1s XPS spectra of samples. (b) Ir L_3-edge XANES spectra of Ir black, $IrCl_3$, IrO_2, Ir_1-NC and Ir_2-ONC. The main characteristics are highlighted by dash lines A and B. (c) The second derivatives of the Ir L_3-edge XANES spectra of IrO_2, Ir_1-NC and Ir_2-ONC. (d) Fourier-transformed k^2-weighted EXAFS spectra. (e) Wavelet transform contours of the Ir L_3-edge of Ir black, $IrCl_3$, IrO_2, Ir_1-NC and Ir_2-ONC.

quantitative analysis manifests that the content of the Ir–N bonding is 24.6% and 26.7% in Ir_1-NC and Ir_2-ONC, respectively (Table S1, ESI†), indicating that Ir_1 and Ir_2 tend to coordinate with N, instead of forming Ir_n nanoclusters or nanoparticles, which agrees with our XRD and HAADF-STEM results. The valence state of Ir in Ir_1-NC and Ir_2-ONC were further examined and compared to that of other reference materials (Fig. S7, ESI†). The Ir $4f_{5/2}$ and $4f_{7/2}$ binding energy peaks located at 65.0 and 62.0 eV, respectively, suggesting that the valence state of Ir is between 0 and +3 in both catalysts.[31,32]

To further investigate the electronic structure and coordination environment of Ir_1-NC and Ir_2-ONC, X-ray absorption near-edge structure (XANES) spectroscopy measurements were performed at the CLÆSS beamline of the ALBA synchrotron.[33] As shown in Fig. 2b, the white-line absorption of Ir_1-NC and Ir_2-ONC shift to the higher energy side with respect to that of Ir black, suggesting that the Ir atoms in Ir_1-NC and Ir_2-ONC carry positive charges, consistent with our XPS results (Fig. S7, ESI†). To distinguish the electronic and structural effects on the white-line position, a more detailed analysis was conducted. Comparing with Ir_1-NC, the white-line of Ir_2-ONC slightly shifts to the lower energy side, which could be attributed to the existence of Ir–Ir bonds in Ir_2-ONC.[34,35] The global shape of the XANES spectra reflects the local geometry of catalysts around the absorber. To this end, we noticed that the Ir L_3-edge XANES spectra of Ir_1-NC and Ir_2-ONC (Fig. 2b) show bumps at 11228.3 and 11264.5 eV (*i.e.*, labels A and B), similar to those of $IrCl_3$ and IrO_2, which is a spectral feature of the octahedral N_6-coordinated Ir complexes.[36–38] The evidence of such an octahedral configuration was additionally confirmed by the second-derivative spectra that can provide more delicate white-line features of the catalysts. As depicted in Fig. 2c, both Ir_1-NC and Ir_2-ONC show a sharper peak with respect to the oxide reference, related to the transition to the e_g states,[39,40] corroborating that Ir atoms coordinate with neighbouring ligand in an octahedral configuration in these catalysts with a charged oxidation state below 4+.

To further illustrate the ligand structure, the k^2 weighted extended X-ray absorption fine structure (EXAFS) spectra were plotted. The Ir_1-NC catalyst shows a prominent peak at 1.56 Å, which results from the first-shell Ir–N scattering path (Fig. 2d). By contrast, the Ir L_3-edge EXAFS spectrum of Ir_2-ONC exhibits a broader peak at 1.59 Å, attributed to the Ir–N/O shell. Quantitative fitting of the EXAFS spectra was further carried out to verify the coordination number of Ir in Ir_1-NC and Ir_2-ONC catalysts. Fig. S8a and b (ESI†) show the existence of Ir–N and Ir–C scattering paths in the first shell and second shell, respectively, in Ir_1-NC, with coordination numbers of 6 and 2 (Table S2, ESI†). In contrast, the Ir_2-ONC catalyst displays an Ir coordination with roughly four N atoms, two O atoms, and another Ir atom (Fig. S8c, d and Table S2, ESI†). Based on the molecular structure of the precursors, which consist of $[Ir(OCH_3)(C_8H_{12})]_2$ with an oxygen-bridge, a bridge model is therefore proposed for Ir_2-ONC. The model comprises two Ir atoms coordinating with each other by sharing two O atoms (*i.e.*, bridges), each of which connects with additional four N atoms. It is hypothesized that the Ir–O and Ir–Ir bonding is inherited from the structural

characteristics of $[Ir(OCH_3)(C_8H_{12})]_2$. Moreover, the wavelet transforms (WT) of the Ir L_3-edge EXAFS oscillations were drawn to distinguish backscattering atoms and show the intensity distribution in both k and R spaces (Fig. 2e).[41] Three peaks appear in the contour plot of Ir_2-ONC, with the most prominent one located at ~6.0 $Å^{-1}$ in k space and ~1.5 Å in R space, corresponding to the Ir–N/O contribution. The other two weak signals appearing at ~2.5 Å and ~3.5 Å in R space are assigned to Ir–Ir/C and Ir–C bonding, respectively. Meanwhile, Ir_2-ONC seems to have an elongated feature at 2.5 Å compared to Ir_1-NC, similar to the Ir–Ir scattering of IrO_2 rather than of metallic Ir.

The electrocatalytic performance of the as-synthesized Ir_2-ONC and other control catalysts toward CER was investigated in 0.1 M $HClO_4$ + 4.0 M NaCl electrolyte in a three-electrode cell. The linear sweep voltammograms (LSVs, Fig. 3a) show that the Ir_2-ONC starts to catalyze the CER at a potential of 1.375 V (@1 mA cm^{-2}), which is only 44 mV higher than the standard reaction potential (E_{CER} = 1.331 V *vs.* NHE), and it can deliver a current density of 10, 50 and 100 mA cm^{-2} at an overpotential of 112, 204 and 247 mV, respectively, much lower than that of Ir_1-NC (157, 288 and 324 mV) and DSA (120, 235 and 363 mV, Fig. 3b). In contrast, the pristine NC support with trace amounts of residual Zn shows significantly lower activity. This indicates that it is the atomically dispersed Ir species, but not the NC support, that are the main active sites for the CER. The Zn residue only has minor, if any, impact on the CER activity. Meanwhile, the polarization curve of Ir_2-ONC in the absence of Cl^- shows a negligible current density up to 1.7 V *vs.* NHE, indicating that the large current density dictated by Ir_2-ONC truly originates from the CER only. We further calculated the Tafel slopes derived from LSV curves to assess the apparent reaction kinetics during CER (Fig. 3c). The Ir_2-ONC shows a Tafel slope of 49.6 mV dec^{-1}, smaller than other control catalysts, confirming that the presence of Ir dinuclear active sites can expedite the CER. Meanwhile, the Tafel slope of 49.6 mV dec^{-1} suggests that the CER on Ir_2-ONC may occur through the Volmer–Heyrovsky mechanism.[23,42] The electrochemical impedance spectroscopy (EIS) measurements also verified the efficient charge transfer of Ir_2-ONC during the CER, as evidenced by its much smaller charge transfer resistance (R_{ct} = 8 Ω) than that of other control samples (Fig. S9, ESI,† R_{ct} = 25 Ω for DSA, R_{ct} = 40 Ω for Ir_1-NC and R_{ct} = 1100 Ω for NC).

To further assess the intrinsic catalytic performance, the electrochemical surface area (ECSA) of Ir_2-ONC and reference samples was estimated and compared through the electrochemical double-layer capacitance (C_{dl}) measurements. As revealed in Fig. S10 (ESI†), Ir_2-ONC shows an ECSA value of 180.1 cm^2, higher than the Ir_1-NC catalyst (131.4 cm^2) and NC support (65.7 cm^2), suggesting that the dispersed dinuclear active sites are conducive to exposing more active sites for electrocatalysis. Nevertheless, the ECSA-normalized specific activity of Ir_2-ONC outperforms that of Ir_1-NC (Fig. S11a, ESI†), indicating the intrinsically higher CER activity of dinuclear active sites. The CER activity was further assessed using the turnover frequency (TOF). As shown in Fig. 3d, the Ir_2-ONC shows a TOF value of 13.51 s^{-1} at E = 1.50 V *vs.* NHE, which is 1.9 and 81.9 times higher than Ir_1-NC and DSA. When comparing with other atomically dispersed CER catalysts reported recently in the literature,[43–47] our Ir_2-ONC catalyst exhibits decent performance and favourably compares to other advanced catalysts (Table S3, ESI†). For noble metal electrocatalysts, mass activity is a critical metric for practical applications, reflecting the effectiveness of noble metal utilization and therefore closely related to the production costs of electrolyzers. The Ir_2-ONC can deliver an exceptionally high mass activity of 14321.6 A g_{Ir}^{-1} at E = 1.50 V *vs.* NHE, significantly higher than that of Ir_1-NC (7696.3 A g_{Ir}^{-1}) and DSA (174.9 A g_{Ir}^{-1}) (Fig. S11b, ESI†).

The electrocatalytic stability is another significant performance indicator of a CER catalyst. The stability of Ir_2-ONC was examined by chronopotentiometry (CP) at a constant current density of 10 mA cm^{-2} and the accelerated stress test (AST). As illustrated in Fig. 3e, the Ir_2-ONC catalyst can catalyze CER continuously at 10 mA cm^{-2} for 20 h with minimal degradation, and the LSV curve remains nearly unchanged after the AST of 40 000 cycles at 100 mV s^{-1}, suggesting excellent stability. The atomic-resolution HAADF-STEM images, XRD, and XPS data of the Ir_2-ONC after the stability test demonstrate that the dispersed Ir dinuclear active sites were well retained on the NC support (Fig. S12, ESI†).

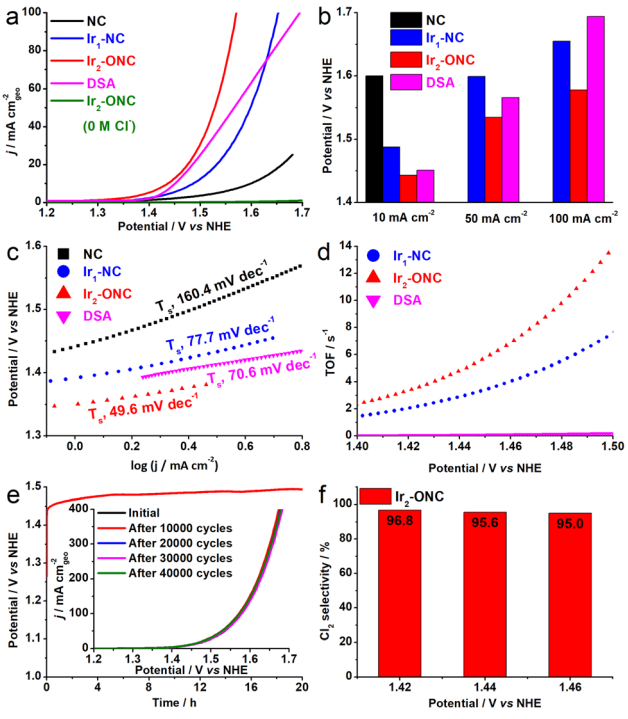

Fig. 3 Electrocatalytic CER performance of Ir_2-ONC and other control samples. (a) LSV polarization curves, recorded at a scan rate of 5 mV s^{-1} in 0.1 M $HClO_4$ + 4 M NaCl. (b) Comparison of the overpotentials of different samples to reach 10, 50 and 100 mA cm^{-2}. (c) Tafel slopes. (d) Calculated TOFs of Ir_1-NC, Ir_2-ONC and DSA. (e) Chronopotentiometric curves of Ir_2-ONC, recorded at a constant current density of 10 mA cm^{-2} in 0.1 M $HClO_4$ + 4 M NaCl. The inset shows the cyclic durability. (f) CER selectivity of Ir_2-ONC at different potentials.

We also assessed the CER selectivity of the catalysts. The ignorable faradaic current of Ir_2-ONC in the absence of NaCl virtually already confirmed its superior selectivity toward CER (Fig. 3a). Nonetheless, to make a quantitative assessment, we employed the iodometric titration method[23,48] to quantify the active chlorine concentrations under different applied potentials. The Ir_2-ONC exhibited a CER faradaic efficiency of 96.8%, 95.6% and 95.0% at 1.42, 1.44 and 1.46 V *vs.* NHE, respectively, demonstrating the excellent selectivity of Ir_2-ONC (Fig. 3f and S13, ESI†).

To further elucidate the origin of the higher CER catalytic activity of Ir_2-ONC with respect to that of Ir_1-NC, density functional theory (DFT) calculations were carried out. According to the XAS results and the molecular structure of the precursors used for the synthesis of Ir_1-NC and Ir_2-ONC, Ir_1-NC is coordinated with six N atoms and Ir_2-ONC adopts a $Ir_2O_2N_8$ coordination with oxygen bridging the Ir_2 dimer. The fine structure of Ir_1-NC and Ir_2-ONC was further elaborated in order to perform DFT calculations. For Ir_1-NC, according to the 18-electron rule, with the d^2sp^3 hybridization, Ir would octahedrally coordinate with 3 negatively charged N^- and 3 N electron lone pairs (Fig. S14, ESI†). Having this in mind, several possible Ir_1N_6 configurations are proposed (Fig. S15, ESI†), where the Ir single atom is forced to bond with the pyrrolic N (negatively charged) and pyridinic N (lone pair) doped graphene model, as well as the methylimidazole (Im, lone pair) and its anion (Im^-, negatively charged). It is worth noting that the methylimidazole is supposed to result from the precursor used in catalyst synthesis, which represents a typical coordination of N lone pairs perpendicular to the support plane, so does its anion. By comparing the catalyst formation energy (E_f), *i.e.*, the substitution energy of Ir from the precursor to the final catalyst, the Ir_1-NC catalyst with two $N_{(pyrrole-)}$, two $N_{(pyridine)}$, 1 $N_{(Im)}$ and 1 $N_{(Im-)}$ was found to be the most stable configuration ($E_f = -0.37$ eV), while other possible combinations give rise to unfavorable formation energies of over 1 eV (Fig. S15, ESI†). Therefore, this stable Ir_1N_6 configuration was adopted in DFT calculations. Similarly, the most stable configuration of $Ir_2O_2N_8$ was also found out. As shown in Fig. S16 (ESI†), the model showing the Ir_2 dimer coordinated with two bridge O, four $N_{(pyrrole-)}$ and four $N_{(Im)}$ has the lowest E_f value (−1.69 eV) among all possible configurations, and therefore is selected for subsequent DFT calculations. It is interesting to note that the E_f of $Ir_2O_2N_8$ is substantially lower than the double of the E_f of Ir_1N_6, which implies that the Ir_2 precursor molecules can be anchored to the carbon support more favorably, rationalizing the presence of Ir dinuclear sites in Ir_2-ONC (Fig. 1 and 2).

Based on the obtained stable Ir_1N_6 and $Ir_2O_2N_8$ configurations, the free energy profiles of the catalysts toward CER were calculated at $U = 1.36$ V (Fig. 4a and S17, ESI†). As the N and O sites in $Ir_2O_2N_8$ are fully coordinated, the calculations show that in the Volmer step Cl^- ions would bind directly on Ir atoms, as proposed in previous reports on SACs,[44,46,49] The free energy change of Cl substitution-coordination on $Ir_2O_2N_8$ ($Im^*Im^* + Cl^- \rightarrow Im^*Cl^* + Im + e^-$) is only 0.01 eV, while that on Ir_1N_6 ($Im^* + Cl^- \rightarrow Cl^* + Im + e^-$) is much higher, amounting to 0.38 eV. This indicates that the $Ir_2O_2N_8$ configuration has

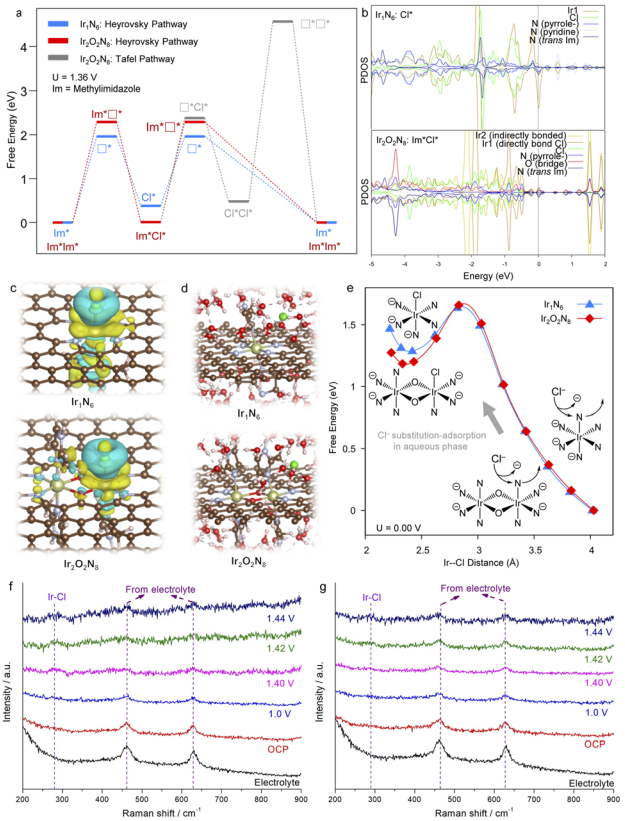

Fig. 4 Computational analysis of the Ir_1N_6 and $Ir_2O_2N_8$ configurations for CER. (a) The free energy profiles of the chlorine evolution reaction. (b) The projection density of state (PDOS) analysis of the Cl adsorption state. (c) The binding electron density difference between the Cl atom and the catalyst. Electron depletion and accumulation are depicted by yellow and blue, plotted with values of ±0.001 |e| $Å^{-3}$. The light green, light blue, red, brown, white and green spheres represent Ir, N, O, C, H and Cl, respectively. (d) 3D models surrounded by explicit solvent water molecules used for AIMD simulations. The color code is the same as that in panel (c). (e) The corresponding free energy curve of Cl^- substitution and adsorption steps simulated by constrained AIMD in aqueous solution. *In situ* Raman spectra collected on (f) Ir_2-ONC and (g) Ir_1-NC catalysts from OCP to 1.44 V *vs.* NHE. Electrolyte: 0.1 M $HClO_4$ + 4 M NaCl.

a higher activity, from the thermodynamics perspective of the Heyrovsky pathway. Furthermore, the Tafel step on $Ir_2O_2N_8$ ($Im^*Cl^* + Cl^- \rightarrow Cl^*Cl^* + Im + e^-$) is found to be endothermic with a free energy change of 0.47 eV, and more strikingly the Cl_2 dissociation energy is around 4 eV ($Cl^*Cl^* \rightarrow \square^*\square^* + Cl_2$), which is energy-demanding. Therefore, the Heyrovsky process, instead of the Tafel process, is more likely to happen during CER, which is in good agreement with our experimental observation (Fig. 3c). It is worth mentioning that the Ir metal center is fully coordinated in the catalyst, so the coordination of Cl likely needs to be accompanied with the dissociation of a N group, *i.e.*, one $N_{(Im)}$. Full dissociation of this $N_{(Im)}$ is not easy to happen for both Ir_1N_6 and $Ir_2O_2N_8$, and it critically depends on the binding strength of Cl on the catalyst. Our DFT calculations indicate that the Cl binding energy on Ir_2-ONC is stronger than that on Ir_1-NC by 0.7 eV, which may result from the distinct

electronic structure of Ir_2-ONC. On the one hand, the projection density of states (PDOS) analysis shows that the Ir–O_{br}–Ir rhombus center participates the Cl binding, lowering its bonding energy (Fig. 4b); on the other hand, the adsorbed Cl likely has additional charge exchange with the delocalized π orbital of the neighboring methylimidazole (Fig. 4c), which strengthens its adsorption. Therefore, the higher chlorophilicity of $Ir_2O_2N_8$ makes Ir_2-ONC a better CER catalyst than Ir_1-NC.

It is worth noting that the full dissociation free energy of $N_{(Im)}$ shown in Fig. 4a is fairly high, given that the calculations were performed in vacuum. In reality, the experiment is carried out in aqueous solution and it is hypothesized that the dissociation of $N_{(Im)}$ and coordination of Cl would take place spontaneously. To validate this hypothesis, *ab initio* molecular dynamics (AIMD) simulations were conducted to mimic the Cl substitution-adsorption step in more realistic conditions, where explicit solvent water with a density 1 g mL^{-1} and one HCl molecule were introduced to surround the catalysts creating an aqueous acidic environment (Fig. 4d). The thermodynamic integration of a serials of constrained AIMD simulations[50,51] shows that both Ir_2-ONC and Ir_1-NC share a very similar free energy curve of $N_{(Im)}$ dissociation, and the free energy barrier is around 1.6 eV (Fig. 4e and S18, ESI†). This suggests not only the thermodynamics but also the kinetics of Cl^- coordination are crucial for the CER, which agrees well with previous studies.[18,23] The $Ir_2O_2N_8$ shows a free energy change of ~0.1 eV more favorable than that of the Ir_1N_6, suggesting stronger Cl adsorption. According to the Boltzmann distribution, this corresponds to 50 times of concentration difference at 300 K. Hence, the AIMD simulations also support that the Ir_2-ONC is a better CER catalyst than Ir_1-NC, which agrees well with the experimental results.

The stronger Cl adsorption on Ir_2-ONC can also be verified experimentally using *in situ* Raman spectroscopy. As revealed in Fig. 4f and g, at the open-circuit potential (OCP), no signal of Ir–Cl bonding is resolved for both Ir_2-ONC and Ir_1-NC, except the one from the electrolyte. As the applied potential increases, a peak at ~285 cm^{-1} signaling the Ir–Cl bonding[52,53] gradually emerges in the Raman spectra of both Ir_1-NC and Ir_2-ONC samples, confirming that intermediate species originates from the substitution-adsorption of Cl^-. Notably, the Ir–Cl signal appears earlier in the Ir_2-ONC than that in the Ir_1-NC, indicating that Ir–Cl can form more readily on the Ir_2-ONC catalyst, which agrees well with the above theoretical simulations.

Conclusions

In summary, we report the synthesis of atomically dispersed Ir dinuclear active sites through a "precursor-preselected" cage-encapsulated strategy. The dinuclear Ir_2-ONC catalyst exhibits an onset potential of 1.375 V *vs.* NHE for CER, a high faradaic efficiency of >95%, a turnover frequency of 13.51 s^{-1} at 1.50 V *vs.* NHE and a high mass activity of 14321.6 A g_{Ir}^{-1} at 1.50 V *vs.* NHE, outperforming the single-atom control catalyst (Ir_1-NC), DSA and many other Ir based catalysts reported in the literature. Our DFT calculations and AIMD simulations in the presence of explicit solvent water disclose that the unique oxygen-bridged $Ir_2O_2N_8$ configuration in Ir_2-ONC catalysts favors the adsorption and coordination of Cl^- and thereby lowers the energy barrier to chlorine evolution, leading to CER performance better than the Ir_1-NC reference catalyst. This work presents the first case study of atomically dispersed dinuclear active sites for CER, and provides insights into the catalytic mechanism of Ir dinuclear active sites toward chlorine evolution. Considering the significantly enhanced mass activity, the Ir_2-ONC catalysts show substantial promise for use as an alternative to the MMO-based catalysts for chlorine evolution.

Data availability

All data required to support the claims made are provided, in the manuscript and its ESI.†

Author contributions

Z. P. Y. and L. L. conceived the experiments; Z. P. Y. synthesized catalysts, performed XRD, SEM, XPS, electrocatalytic tests and wrote the initial manuscript; G. J. X. performed DFT calculations; V. M. D. and L. S. contributed to XAS measurements; A. P. L. carried out TEM characterization; X. Y. X. performed the nitrogen adsorption/desorption porosimetry measurements; Z. X. T. and D. H. X. contributed to the discussion. L. L. contributed to data analyses and wrote the final manuscript. All authors read and agreed on the manuscript. L. L. coordinated the project.

Conflicts of interest

There are no conflicts to declare.

Acknowledgements

L. Liu acknowledges the financial support from the Ministry of Science & Technology of China (Grant No. 22J4021Z311) and the start-up grant of the Songshan Lake Materials Laboratory (Grant No. Y2D1051Z311). G.-J. Xia acknowledges the financial support from NSFC (Grant No. 22203041), Guangdong Basic and Applied Basic Research Foundation, China (Grant No. 2021A1515110406), and Dongguan Key Laboratory of Artificial Intelligence Design for Advanced Materials. The materials characterization was carried out in part using the Advanced Electron Microscopy, Imaging and Spectroscopy (AEMIS) facilities available at INL.

Notes and references

1 *World Chlorine Council Sustainable Progress*, https://worldchlorine.org/wp-content/uploads/2018/10/WCC_Sustainable-Progress_Version-3-2017.pdf, accessed on February 2024.
2 P. Schmittinger, T. Florkiewicz, L. C. Curlin, B. Lüke, R. Scannell, T. Navin, E. Zelfel and R. Bartsch, Chlorine,

Ullmann's Encyclopedia of Industrial Chemistry, Wiley-VCH, Weinheim, 2011.
3 E. Tsolaki and E. Diamadopoulos, *J. Chem. Technol. Biotechnol.*, 2010, **85**, 19–32.
4 T. Brinkmann, G. Giner Santonja, L. Delgado Sancho, F. Schorcht and S. Roudier, *Best available techniques (BAT) reference document for the production of chlor-alkali – Industrial Emissions Directive 2010/75/EU (integrated pollution prevention and control)*, Publications Office of the European Union, Luxembourg, 2014.
5 R. K. B. Karlsson and A. Cornell, *Chem. Rev.*, 2016, **116**, 2982–3028.
6 S. Trasatti, *Electrochim. Acta*, 2000, **45**, 2377–2385.
7 I. A. Moreno-Hernandez, B. S. Brunschwig and N. S. Lewis, *Energy Environ. Sci.*, 2019, **12**, 1241–1248.
8 J. G. Vos, Z. Liu, F. D. Speck, N. Perini, W. Fu, S. Cherevko and M. T. M. Koper, *ACS Catal.*, 2019, **9**, 8561–8574.
9 K. S. Exner, J. Anton, T. Jacob and H. Over, *Angew. Chem., Int. Ed.*, 2014, **53**, 11032–11035.
10 D. Wintrich, D. Öhl, S. Barwe, A. Ganassin, S. Möller, T. Tarnev, A. Botz, A. Ruff, J. Clausmeyer, J. Masa and W. Schuhmann, *ChemElectroChem*, 2019, **6**, 3108–3112.
11 T. Arikawa, Y. Murakami and Y. Takasu, *J. Appl. Electrochem.*, 1998, **28**, 511–516.
12 J. Yang, W. H. Li, K. Xu, S. Tan, D. Wang and Y. Li, *Angew. Chem., Int. Ed.*, 2022, **61**, e202200366.
13 S. Li, X. Guo, X. Liu and J. Shui, *ACS Catal.*, 2024, **14**, 1962–1969.
14 Z. Yu, Y. Li, A. Torres-Pinto, A. P. LaGrow, V. M. Diaconescu, L. Simonelli, M. J. Sampaio, O. Bondarchuk, I. Amorim, A. Araujo, A. M. T. Silva, C. G. Silva, J. L. Faria and L. Liu, *Appl. Catal., B*, 2022, **310**, 121318.
15 Z. Yu, C. Si, F. J. Escobar-Bedia, A. P. LaGrow, J. Xu, M. J. Sabater, I. Amorim, A. Araujo, J. P. S. Sousa, L. Meng, J. L. Faria, P. Concepcion, B. Li and L. Liu, *Inorg. Chem. Front.*, 2022, **9**, 4142–4150.
16 Z. Yu, J. Xu, S. Feng, X. Song, O. Bondarchuk, J. L. Faria, Y. Ding and L. Liu, *New J. Chem.*, 2021, **45**, 5770–5774.
17 Y. Wang, H. Su, Y. He, L. Li, S. Zhu, H. Shen, P. Xie, X. Fu, G. Zhou, C. Feng, D. Zhao, F. Xiao, X. Zhu, Y. Zeng, M. Shao, S. Chen, G. Wu, J. Zeng and C. Wang, *Chem. Rev.*, 2020, **120**, 12217–12314.
18 K. S. Exner, J. Anton, T. Jacob and H. Over, *Angew. Chem., Int. Ed.*, 2016, **55**, 7501–7504.
19 I. Sohrabnejad-Eskan, A. Goryachev, K. S. Exner, L. A. Kibler, E. J. M. Hensen, J. P. Hofmann and H. Over, *ACS Catal.*, 2017, **7**, 2403–2411.
20 Z. Yu, C. Si, A. P. LaGrow, Z. Tai, W. A. Caliebe, A. Tayal, M. J. Sampaio, J. P. S. Sousa, I. Amorim, A. Araujo, L. Meng, J. L. Faria, J. Xu, B. Li and L. Liu, *ACS Catal.*, 2022, **12**, 9397–9409.
21 T. Ding, X. Liu, Z. Tao, T. Liu, T. Chen, W. Zhang, X. Shen, D. Liu, S. Wang, B. Pang, D. Wu, L. Cao, L. Wang, T. Liu, Y. Li, H. Sheng, M. Zhu and T. Yao, *J. Am. Chem. Soc.*, 2021, **143**, 11317–11324.
22 W. Zhang, Y. Chao, W. Zhang, J. Zhou, F. Lv, K. Wang, F. Lin, H. Luo, J. Li, M. Tong, E. Wang and S. Guo, *Adv. Mater.*, 2021, **33**, 2102576.
23 T. Lim, G. Y. Jung, J. H. Kim, S. O. Park, J. Park, Y.-T. Kim, S. J. Kang, H. Y. Jeong, S. K. Kwak and S. H. Joo, *Nat. Commun.*, 2020, **11**, 412.
24 Y. Yao, L. Zhao, J. Dai, J. Wang, C. Fang, G. Zhan, Q. Zheng, W. Hou and L. Zhang, *Angew. Chem., Int. Ed.*, 2022, **61**, e202208215.
25 S. Gadipelli and Z. X. Guo, *ChemSusChem*, 2015, **8**, 2123–2132.
26 J. S. Bates, F. Khamespanah, D. A. Cullen, A. A. Al-Omari, M. N. Hopkins, J. J. Martinez, T. W. Root and S. S. Stahl, *J. Am. Chem. Soc.*, 2022, **144**, 18797–18802.
27 Z. Zeng, L. Y. Gan, H. Bin Yang, X. Su, J. Gao, W. Liu, H. Matsumoto, J. Gong, J. Zhang, W. Cai, Z. Zhang, Y. Yan, B. Liu and P. Chen, *Nat. Commun.*, 2021, **12**, 4088.
28 Y. Wang, Z. Li, P. Zhang, Y. Pan, Y. Zhang, Q. Cai, S. R. P. Silva, J. Liu, G. Zhang, X. Sun and Z. Yan, *Nano Energy*, 2021, **87**, 106147.
29 L. Jiao, J. Zhu, Y. Zhang, W. Yang, S. Zhou, A. Li, C. Xie, X. Zheng, W. Zhou, S. H. Yu and H. L. Jiang, *J. Am. Chem. Soc.*, 2021, **143**, 19417–19424.
30 W. Ren, X. Tan, W. Yang, C. Jia, S. Xu, K. Wang, S. C. Smith and C. Zhao, *Angew. Chem., Int. Ed.*, 2019, **58**, 6972–6976.
31 Z. Yu, J. Xu, Y. Li, B. Wei, N. Zhang, Y. Li, O. Bondarchuk, H. Miao, A. Araujo, Z. Wang, J. L. Faria, Y. Liu and L. Liu, *J. Mater. Chem. A*, 2020, **8**, 24743–24751.
32 Z. Li, Y. Chen, S. Ji, Y. Tang, W. Chen, A. Li, J. Zhao, Y. Xiong, Y. Wu, Y. Gong, T. Yao, W. Liu, L. Zheng, J. Dong, Y. Wang, Z. Zhuang, W. Xing, C. T. He, C. Peng, W. C. Cheong, Q. Li, M. Zhang, Z. Chen, N. Fu, X. Gao, W. Zhu, J. Wan, J. Zhang, L. Gu, S. Wei, P. Hu, J. Luo, J. Li, C. Chen, Q. Peng, X. Duan, Y. Huang, X. M. Chen, D. Wang and Y. Li, *Nat. Chem.*, 2020, **12**, 764–772.
33 L. Simonelli, C. Marini, W. Olszewski, M. Ávila Pérez, N. Ramanan, G. Guilera, V. Cuartero and K. Klementiev, *Cogent Phys.*, 2016, **3**, 1231987.
34 Y. Li, C. Chen, R. Cao, Z. Pan, H. He and K. Zhou, *Appl. Catal., B*, 2020, **268**, 118747.
35 W. Ye, S. Chen, Y. Lin, L. Yang, S. Chen, X. Zheng, Z. Qi, C. Wang, R. Long, M. Chen, J. Zhu, P. Gao, L. Song, J. Jiang and Y. Xiong, *Chem*, 2019, **5**, 2865–2878.
36 A. A. Guda, S. A. Guda, A. Martini, A. N. Kravtsova, A. Algasov, A. Bugaev, S. P. Kubrin, L. V. Guda, P. Šot, J. A. van Bokhoven, C. Copéret and A. V. Soldatov, *npj Comput. Mater.*, 2021, **7**, 203.
37 P. Liu, X. Huang, D. Mance and C. Copéret, *Nat. Catal.*, 2021, **4**, 968–975.
38 K. Mori, M. Tottori, K. Watanabe, M. Che and H. Yamashita, *J. Phys. Chem. C*, 2011, **115**, 21358–21362.
39 J. H. Choy, D. K. Kim, G. Demazeau and D. Y. Jung, *J. Phys. Chem.*, 1994, **98**, 6258–6262.
40 J. H. Choy, D. K. Kim, S. H. Hwang, G. Demazeau and D. Y. Jung, *J. Am. Chem. Soc.*, 1995, **117**, 8557–8566.
41 H. Funke, A. C. Scheinost and M. Chukalina, *Phys. Rev. B*, 2005, **71**, 094110.

42 S. Trasatti, *Electrochim. Acta*, 1987, **32**, 369–382.
43 T. Lim, J. H. Kim, J. Kim, D. S. Baek, T. J. Shin, H. Y. Jeong, K.-S. Lee, K. S. Exner and S. H. Joo, *ACS Catal.*, 2021, **11**, 12232–12246.
44 Y. Liu, C. Li, C. Tan, Z. Pei, T. Yang, S. Zhang, Q. Huang, Y. Wang, Z. Zhou, X. Liao, J. Dong, H. Tan, W. Yan, H. Yin, Z.-Q. Liu, J. Huang and S. Zhao, *Nat. Commun.*, 2023, **14**, 2475.
45 J. Cho, T. Lim, H. Kim, L. Meng, J. Kim, S. Lee, J. H. Lee, G. Y. Jung, K. S. Lee, F. Viñes, F. Illas, K. S. Exner, S. H. Joo and C. H. Choi, *Nat. Commun.*, 2023, **14**, 3233.
46 M. Ha, P. Thangavel, N. K. Dang, D. Y. Kim, S. Sultan, J. S. Lee and K. S. Kim, *Small*, 2023, **19**, 2300240.
47 L. Quan, X. Chen, J. Liu, S. Fan, B. Y. Xia and B. You, *Adv. Funct. Mater.*, 2023, **33**, 2307643.
48 J. G. Vos and M. T. M. Koper, *J. Electroanal. Chem.*, 2018, **819**, 260–268.
49 J. Wang, L. Zhao, Y. Zou, J. Dai, Q. Zheng, X. Zou, L. Hu, W. Hou, R. Wang, K. Wang, Y. Shi, G. Zhan, Y. Yao and L. Zhang, *J. Am. Chem. Soc.*, 2024, **146**, 11152–11163.
50 J. Z. Peng, Y. L. Li, Y. T. Cheng, F. Z. Li, B. Cao, Q. Wang, X. Yue, G. T. Lai, Y. G. Wang and J. Gu, *Carbon Energy*, 2024, e506.
51 Y. Qiao, G. J. Xia, W. Cao, K. H. Zeng, Q. L. Guo, X. F. Yang, A. Q. Wang and Y. G. Wang, *J. Catal.*, 2023, **427**, 115114.
52 S. C. Chan, S. C. Fung and J. H. Sinfelt, *J. Catal.*, 1988, **113**, 164–171.
53 M. F. Mrozek and M. J. Weaver, *J. Am. Chem. Soc.*, 2000, **122**, 150–155.